Volume 322B, Number 3 May 15, 2014

JEZ

JOURNAL OF EXPERIMENTAL ZOOLOGY

PART B

MOLECULAR AND DEVELOPMENTAL EVOLUTION

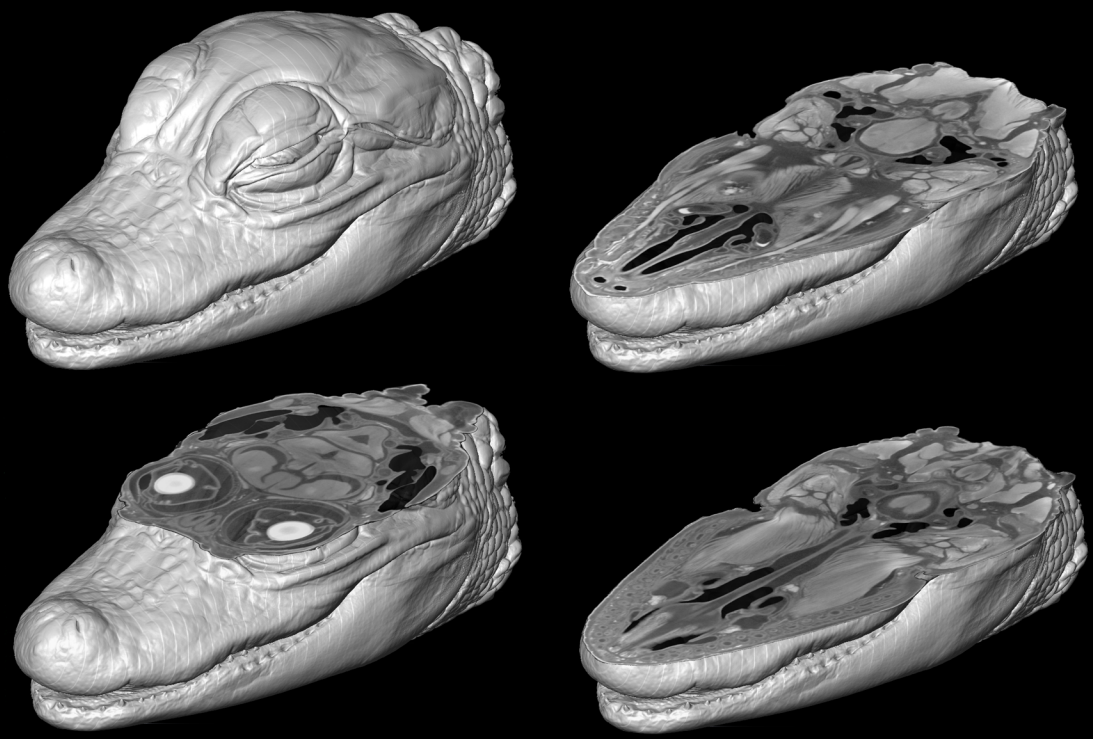

Officially sponsored by
The Society for Integrative
and Comparative Biology

WILEY Blackwell
ISSN 1552-5007

RESEARCH ARTICLE

Iodine-Enhanced Micro-CT Imaging: Methodological Refinements for the Study of the Soft-Tissue Anatomy of Post-Embryonic Vertebrates

JOURNAL OF EXPERIMENTAL ZOOLOGY PART B MOLECULAR AND DEVELOPMENTAL EVOLUTION

PAUL M. GIGNAC[1,2]* AND NATHAN J. KLEY[1]

[1]Department of Anatomical Sciences, Stony Brook University, Stony Brook, New York
[2]Department of Anatomy and Cell Biology, Oklahoma State University Center for Health Sciences, Tulsa, Oklahoma

ABSTRACT

The now widespread use of non-destructive X-ray computed tomography (CT) and micro-CT (μCT) has greatly augmented our ability to comprehensively detail and quantify the internal hard-tissue anatomy of vertebrates. However, the utility of X-ray imaging for gaining similar insights into vertebrate soft-tissue anatomy has yet to be fully realized due to the naturally low X-ray absorption of non-mineralized tissues. In this study, we show how a wide diversity of soft-tissue structures within the vertebrate head—including muscles, glands, fat deposits, perichondria, dural venous sinuses, white and gray matter of the brain, as well as cranial nerves and associated ganglia—can be rapidly visualized in their natural relationships with extraordinary levels of detail using iodine-enhanced (i-e) μCT imaging. To date, Lugol's iodine solution (I_2KI) has been used as a contrast agent for μCT imaging of small invertebrates, vertebrate embryos, and certain isolated parts of larger, post-embryonic vertebrates. These previous studies have all yielded promising results, but visualization of soft tissues in smaller invertebrate and embryonic vertebrate specimens has generally been more complete than that for larger, post-embryonic vertebrates. Our research builds on these previous studies by using high-energy μCT together with more highly concentrated I_2KI solutions and longer staining times to optimize the imaging and differentiation of soft tissues within the heads of post-embryonic archosaurs (*Alligator mississippiensis* and *Dromaius novaehollandiae*). We systematically quantify the intensities of tissue staining, demonstrate the range of anatomical structures that can be visualized, and generate a partial three-dimensional reconstruction of alligator cephalic soft-tissue anatomy. *J. Exp. Zool. (Mol. Dev. Evol.) 322B:166–176, 2014.* © 2014 Wiley Periodicals, Inc.

J. Exp. Zool. (Mol. Dev. Evol.) 322B:166–176, 2014

How to cite this article: Gignac PM, Kley NJ. 2014. Iodine-enhanced micro-CT imaging: Methodological refinements for the study of the soft-tissue anatomy of post-embryonic vertebrates. J. Exp. Zool. (Mol. Dev. Evol.) 322B:166–176.

Modern imaging methods vastly enhance our ability to appreciate complex anatomical relationships and to harness these relationships for understanding the nature of developmental and evolutionary changes in morphology. Among such methods of visualization, the now widespread use of non-destructive X-ray computed tomography (CT) and micro-CT (μCT) has greatly augmented our ability to comprehensively detail and quantify the morphology of dense vertebrate tissues such as bone, dentine, and enamel (e.g., van Rietbergen et al., '95; Rhodes et al., '99; Rayfield

Grant sponsor: National Science Foundation; grant number: NSF IOS-0749750; grant sponsor: Stony Brook University Department of Anatomical Sciences.

*Correspondence to: Paul M. Gignac, Department of Anatomy and Cell Biology, Oklahoma State University, Center for Health Sciences, Tulsa, OK 74107. E-mail: paul.gignac@okstate.edu

Received 21 May 2013; Revised 29 October 2013; Accepted 6 January 2014

DOI: 10.1002/jez.b.22561

Published online 30 January 2014 in Wiley Online Library (wileyonlinelibrary.com).

et al., 2001; Witmer, 2004; Moazen et al., 2008). These advances have led to the identification of novel phylogenetic characters (e.g., Rae et al., 2002; Bloch and Silcox, 2006; Gauthier et al., 2012), new frameworks for functional inference (e.g., XROMM; Brainerd et al., 2010), finite element analyses of complex biological shapes (e.g., Ross, 2005), and sophisticated means by which to reconstruct soft tissues in long-extinct taxa (e.g., Witmer et al., 2008), among other innovations.

Similar insights into vertebrate soft-tissue anatomy using X-ray imaging, however, have yet to be fully realized due to the naturally low X-ray absorption of non-mineralized tissues. Recent work by Metscher (2009a,b; see also Faulwetter et al., 2013; Pauwels et al., 2013) has sought to address this limitation directly. Through experimental evaluation of several contrast agents for use in μCT studies, Metscher (2009b) demonstrated that an aqueous solution of Lugol's iodine (I_2KI) is among the most effective means for rapidly differentiating a diversity of soft tissue types. These comparisons have helped to expand the utility of iodine-enhanced (i-e) CT methods for imaging soft tissues by revealing the remarkable clarity with which epithelial, muscular, and neural anatomy can be visualized in a range of very small specimens. These specimens have included invertebrates and vertebrate embryos (e.g., hatchling squid, embryonic chicks, frogs, and mice; Metscher, 2009a,b), as well as comparably small vertebrate hatchlings (e.g., pike fry; Metscher, 2009a). Given the superlative quality and detail of the imaging of these specimens, it is somewhat surprising that i-e μCT has not yet become adopted more widely.

More recently, others have begun to build upon Metscher's work by applying his protocols with Lugol's iodine solution to larger, post-embryonic vertebrate specimens, including the heads (Cox and Jeffery, 2011; Cox et al., 2011; Jeffery et al., 2011), hearts (Degenhardt et al., 2010; Stephenson et al., 2012), and whole neonatal bodies (Tobita et al., 2010) of rodents, the head of a yearling alligator (Tsai and Holliday, 2011; George and Holliday, 2013), the penises of bats (Herdina et al., 2010), and the syringeal muscles of birds (Düring et al., 2013). Although these studies have been successful in imaging and differentiating some types of soft tissues (most notably muscles), none have achieved the level of detail that Metscher (2009a,b) demonstrated with his much smaller specimens. In particular, the larger sizes of post-embryonic vertebrates appear to make complete staining of some tissues more difficult, resulting in the incomplete visualization of deeply situated structures, such as the brain (Jeffery et al., 2011; Tsai and Holliday, 2011).

In this paper, we outline and evaluate a revised protocol for i-e μCT imaging of post-embryonic vertebrates that builds upon and extends the methods of recent pioneering studies (Metscher, 2009a,b; Degenhardt et al., 2010; Herdina et al., 2010; Tobita et al., 2010; Cox and Jeffery, 2011; Jeffery et al., 2011; Tsai and Holliday, 2011; Stephenson et al., 2012; Düring et al., 2013; George and Holliday, 2013) to facilitate more complete visualization of a wider array of soft tissue types in larger specimens. Specifically, we use the heads of young American alligators (*Alligator mississippiensis*) and emus (*Dromaius novaehollandiae*) to demonstrate that i-e μCT imaging of larger, post-embryonic vertebrate specimens is enhanced significantly, beyond the results of most previous work, by using longer staining times at higher concentrations of Lugol's iodine solution, together with higher energy X-rays. Our results include clear differentiation of muscular and glandular tissues, fat deposits, dural venous sinuses, and epithelial structures, as well as both myelinated and non-myelinated components of the central and peripheral nervous systems. This work therefore sets the stage for the detailed imaging of soft-tissue anatomy in a much broader diversity of vertebrate taxa using i-e μCT methodologies.

MATERIALS AND METHODS

Specimen Fixation and Staining

Six live American alligators (*Alligator mississippiensis*), ranging in body mass from 52 to 474 g, were obtained from the Louisiana Department of Wildlife and Fisheries in Cameron Parish, Louisiana. Specimens were euthanized at between 5 and 18 months of age with intraperitoneal injections of sodium pentobarbital (150 mg/kg) (as approved by the Stony Brook University Institutional Animal Care and Use Committee [IACUC protocol #236370-1]). In addition, two 2-week-old emus (*Dromaius novaehollandiae*), ranging in body mass from 267 to 469 g, were obtained as freshly dead specimens from the Songline Emu Farm (Gill, MA, USA).

The six alligator specimens ranged in standard head length from 39.1 to 79.6 mm and were manually decapitated between the second and third cervical vertebrae. All were immediately fixed in 10% neutral buffered formalin for 2 weeks, and five of the six specimens were then transferred directly into an aqueous solution of 11.25% Lugol's iodine (I_2KI) (i.e., 3.75% w/v of I_2 and 7.5% w/v of KI). In solution, iodine (I_2) and potassium iodide (KI) form into iodine trimers (I_3^+) and potassium ions (K^-) (Degenhardt et al., 2010). Although the staining mechanisms remain incompletely understood, it is clear that the iodine trimers bind to carbohydrates such as glycogen (Bock and Shear, '72; Metscher, 2009b), as well as to lipids (this study; see below), which are naturally present in varying amounts within many types of vertebrate soft tissues. Differences in staining durations result in differences in total iodine uptake, which should, in turn, correlate with the relative degree of soft-tissue differentiation in μCT images. Therefore, to examine the effect of staining time on imaging quality, five alligator specimens were stained with Lugol's iodine solution for varying durations of 1 ($n = 1$), 2 ($n = 5$), or 4 ($n = 1$) weeks. (As indicated in Table 1, two of these five specimens were each μCT-scanned a second time after being stained for an additional 1 or 2 weeks, thus yielding a sample size of seven i-e alligator scans.) The sixth alligator specimen was also μCT-scanned but remained

Table 1. Summary of staining and μCT variables for the *Alligator mississippiensis* and *Dromaius novaehollandiae* specimens examined in this study.

Specimen ID	Species	Duration in 11.25% I_2KI (days)	Peak X-ray-tube voltage (kV)	Peak X-ray-tube amperage (μA)	Cu filter thickness (mm)	Isometric voxel size (μm)
Am1	*A. mississippiensis*	7	150	130	0.1	31.7
Am1	*A. mississippiensis*	14	200	135	0.3	32.4
Am3	*A. mississippiensis*	14	190	135	0.5	33.8
Am8	*A. mississippiensis*	14	200	135	0.3	38.3
Am9	*A. mississippiensis*	14	190	135	0.5	33.8
Am9	*A. mississippiensis*	28	160	145	0.2	35.7
Am13	*A. mississippiensis*	14	200	135	0.3	31.6
Am15	*A. mississippiensis*	0	190	135	0.5	33.8
Dn1	*D. novaehollandiae*	14	180	145	0.1	33.7
Dn1	*D. novaehollandiae*	28	130	190	0.1	38.4
Dn2	*D. novaehollandiae*	14	180	145	0.1	33.7
Dn2	*D. novaehollandiae*	21	170	190	0.1	37.2

unstained as a control (see Fig. 1). Following this protocol, two emu specimens (standard head lengths of 60.3 and 63.4 mm) were manually decapitated between the third and fourth cervical vertebrae, fixed in 10% neutral buffered formalin for 2 weeks, and then transferred into a bath of 11.25% Lugol's iodine solution for 2 ($n = 2$), 3 ($n = 1$), or 4 ($n = 1$) weeks. (As for two of our alligator specimens, both emu specimens were μCT-scanned twice throughout the duration of the staining process. Details are listed in Table 1.)

μCT Scanning

Stained specimens were removed from the Lugol's solution, rinsed with tap water to remove excess stain, blotted dry, sealed individually in polyethylene bags to prevent dehydration, and then loaded into plastic mounting units for scanning. All stained specimens, as well as one unstained alligator (also bagged airtight and loaded into a plastic mounting unit), were μCT-scanned at the Microscopy and Imaging Facility at the American Museum of Natural History (New York, NY, USA), using a 2010 GE phoenix v|tome|x s240 high-resolution microfocus computed tomography system (General Electric, Fairfield, CT, USA). A standard X-ray scout image was obtained prior to scanning to confirm specimen orientation and define the scan volume. All scans were performed at 130–200 kV and 130–190 μA, using 0.1–0.5 mm copper filters, air as the background medium, and a molybdenum target. All specimens were scanned at isometric voxel sizes of 30–40 μm, and slices were assembled on an HP z800 workstation (Hewlett-Packard, Palo Alto, CA, USA) running VG Studio Max (Volume Graphics GmbH, Heidelberg, Germany). Scan times ranged from 90 to 300 min depending on specimen size. Scanning parameters, in addition to staining durations, for all specimens examined are summarized in Table 1.

Quantification of Tissue-Specific Brightness and Contrast Levels in μCT Images

To test which staining durations resulted in the greatest levels of contrast between different tissue types in i-e μCT images, we quantified pixel brightness (in units of grayscale values [GVs] from 0 to 255, ranging from black to white, respectively) for homologous structures in each set of alligator scans. We used frontal slices at 8-bit color depth taken through the level of the optic chiasm, in which all major types of cephalic soft tissues were visible (see Fig. 2A, right). First, all non-tissue background (i.e., air) was removed from single-slice TIFF images using the Instant Alpha tool in Preview (Apple, Cupertino, CA, USA). Next, the resultant image files containing only specimen information were opened in Adobe Photoshop (Adobe Systems, Mountain View, CA, USA) to measure pixel brightness. Specifically, mean grayscale values (±1 SD) were obtained using the histogram tool in Adobe Photoshop for (1) each entire μCT TIFF slice, and (2) 5×5 pixel squares sampled within specific anatomical structures. The latter samples were selected as being representative of certain specific classes of vertebrate tissues types: external lamina of the jugal (cortical bone), orbital fat pad (adipose tissue), Harderian gland (exocrine glandular tissue), gray matter of the diencephalon (non-myelinated central nervous tissue), root of the trigeminal nerve (myelinated peripheral nervous tissue), maxillomandibular (CN V_{2+3}) ganglion (non-myelinated peripheral nervous tissue), and the *M. pseudotemporalis* (striated skeletal muscle) (see Fig. 2). Adobe Photoshop calculates the mean grayscale value and corresponding SD for each square of sampled pixels automatically. To determine the characteristic grayscale value for each tissue type, the mean values for each pixel sample of homologous tissues under the same staining regime were averaged. Pooled standard deviations for these means were then

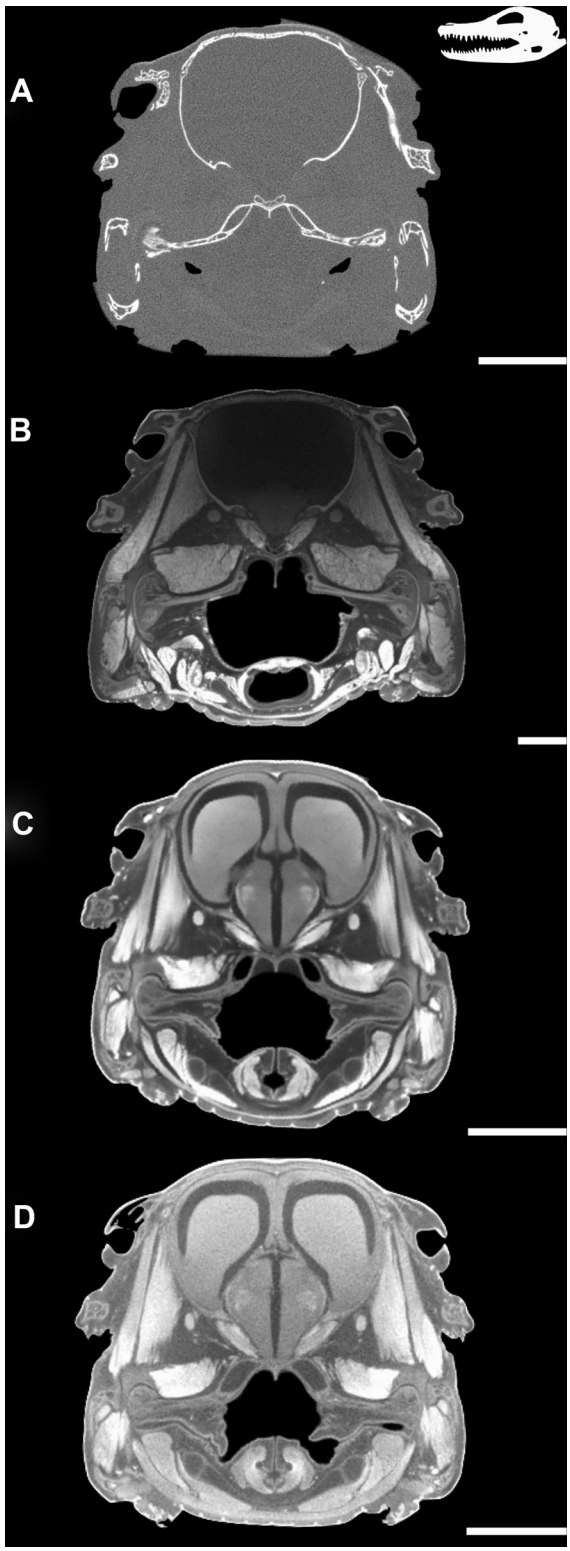

Figure 1. X-ray μCT slices through the heads of four post-hatchling American alligators (*Alligator mississippiensis*), illustrating the effects of I_2KI staining duration on the imaging and differentiation of soft anatomical structures. (**A**) Transverse slice through the anterior portion of the jaw adductor chamber of an unstained specimen (22.5 mm head width [HW]). Note that only bone can be visualized clearly in this control specimen. (**B–D**) Transverse slices through the heads of three I_2KI-stained specimens (39.7 mm HW, 21.5 mm HW, and 21.7 mm HW, respectively), taken in the same approximate plane as that shown in A, illustrating the effects of staining in an 11.25% I_2KI solution for 1 (B), 2 (C), or 4 (D) weeks. Note that with these specimens, optimum contrast levels were achieved after 2 weeks of staining (C); shorter durations resulted in incomplete and uneven staining (B), whereas longer durations resulted in decreased levels of contrast due to the soft tissues becoming oversaturated with iodine (D). Scale bars = 0.5 cm.

calculated by squaring each SD to derive variance, averaging the variances for like tissues at like staining durations, and then taking the square root of those averaged variances (Headrick, 2010). Finally, the contrast level of each tissue type (relative to the entire μCT TIFF slice from which it was sampled) was determined using the following equation:

$$C = 100 \times \frac{X_t - X_{mean}}{X_{mean}} \quad (1)$$

where C is contrast difference as a percentage; X_t is the mean grayscale value of the sample box for a given tissue; X_{mean} is the mean grayscale value for the entire TIFF slice. Contrast difference is a unitless measure, represented here as a percentage value in comparison to the mean brightness of the entire corresponding TIFF slice. Positive values are brighter than the mean, and negative values are darker. Comparing contrast levels in this way allows for us to determine if certain tissues are more clearly visualized under certain preparation regimes. No adjustments were made to the brightness or contrast levels of the frontal view TIFF slices prior to taking these measurements. Grayscale and contrast values are summarized in Table 2.

3D Digital Reconstruction

A selected subset of gross anatomical structures, including the brain, six extrinsic ocular muscles, and cranial nerves I–VI of one alligator were identified and reconstructed digitally using Avizo software (Visualization Sciences Group, Burlington, MA, USA) running on an iMac computer (Apple). The anatomical relationships of these structures were then verified using previous literature accounts and standard gross dissection techniques.

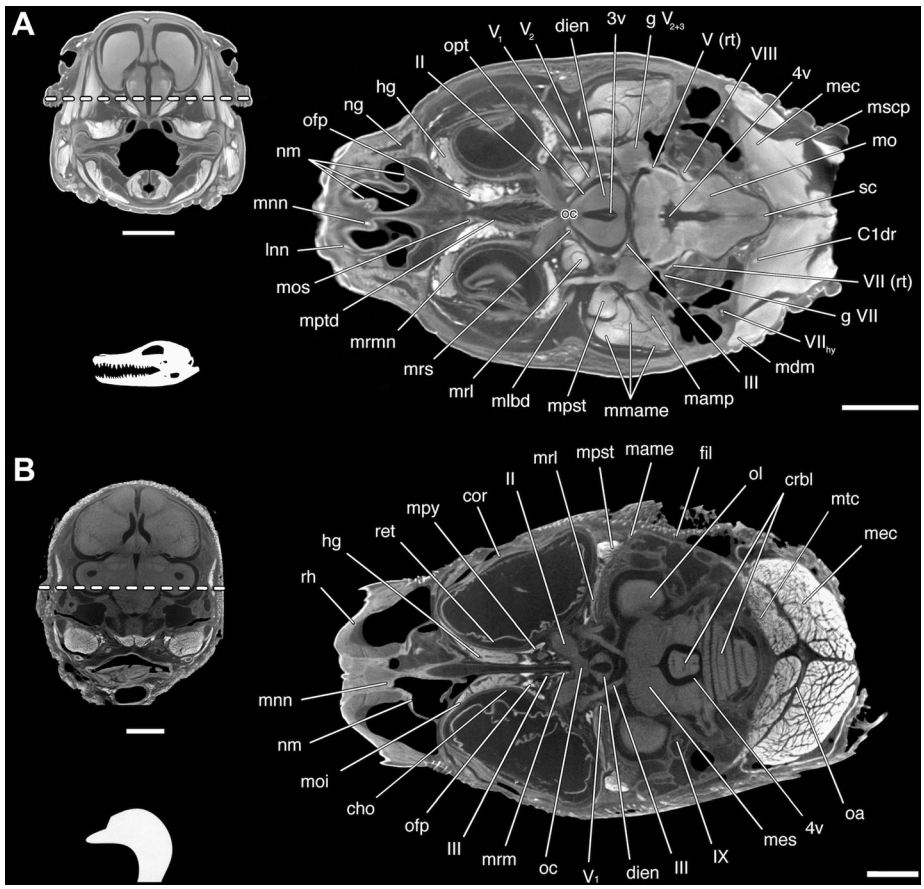

Figure 2. X-ray μCT slices through the heads of (**A**) a post-hatchling (21.5 mm head width) American alligator (*Alligator mississippiensis*), and (**B**) a post-hatchling (29.8 mm head width) emu (*Dromaius novaehollandiae*), illustrating the extraordinary diversity of soft anatomical structures that can be clearly visualized via iodine-enhanced (i-e) μCT imaging. Each specimen was stained in an 11.25% Lugol's iodine (I_2KI) solution for either (A) 2 or (B) 4 weeks. The planes of the frontal slices on the right are indicated by the dashed lines across the transverse slices on the left. Scale bars = 0.5 cm. 3v, third ventricle; 4v, fourth ventricle; cor, cornea; cho, choroid; crbl, cerebellum; C1dr, dorsal ramus of first cervical spinal nerve; dien, diencephalon; fil, cranial filoplume; g V_{2+3}, maxillomandibular ganglion; g VII, geniculate ganglion; hg, Harderian gland; lnn, lateral nasal nerve; mame, *M. adductor mandibulae externus*; mamp, *M. adductor mandibulae posterior*; mdm, *M. depressor mandibulae*; mec, *M. epistropheo-capitis*; mes, mesencephalon; mlbd, *M. levator bulbi, pars dorsalis*; mmame, *Mm. adductores mandibulae externus* (*partes superficialis, medialis, et profundus*); mnn, medial nasal nerve; mo, medulla oblongata; moi, *M. obliquus inferior*; mos, *M. obliquus superior*; mpst, *M. pseudotemporalis*; mptd, *M. pterygoideus dorsalis*; mpy, *M. pyramidalis*; mrl, *M. rectus lateralis*; mrm, *M. rectus medialis*; mrmn, *M. retractor membranae nictitantis*; mrs, *M. rectus superior*; mscp, *M. spino-capitis posticus*; mtc, *M. transversospinalis capitis*; ng, nasal gland; nm, nasal mucosa; oa, occipital artery; oc, optic chiasm; ofp, orbital fat pad; ol, optic lobe; opt, optic tract; ret, retina; rh, rhamphotheca; sc, spinal cord; II, optic nerve; III, oculomotor nerve; V (rt), root of trigeminal nerve; V_1, ophthalmic division of trigeminal nerve; V_2, maxillary division of trigeminal nerve; VII (rt), root of facial nerve; VII_{hy}, hyomandibular ramus of facial nerve; VIII, vestibulocochlear nerve; IX, glossopharyngeal nerve.

RESULTS

We tested for optimal staining duration by comparing μCT scans of post-hatchling alligator heads that had been stained in an 11.25% Lugol's iodine (I_2KI) solution for 1, 2, or 4 weeks (Fig. 1B–D). After 1 week of staining, we found superficial tissues (e.g., hyobranchial muscles, distal branches of peripheral nerves) to be moderately well contrasted, but tissues located more deeply within the head, such as the brain, were poorly contrasted or not even visible. In general, μCT scans of our 1-week preparation (Fig. 1B) are comparable to those of the head of a yearling American

Table 2. Comparison of percent mean (±pooled SD; see Materials and Methods section) tissue contrast (C) (see Equation 1) for homologous soft-tissue structures in frontal μCT slices of an unstained *Alligator mississippiensis* specimen and those prepared under three different I_2KI staining durations.

Duration	Whole specimen (GV)	Cortical bone (C)	Fat (C)	Gland (C)	nM CNS (C)	nM PNS (C)	M PNS (C)	Skeletal muscle (C)
Unstained ($n = 1$)	106.0 ± 81.5	38.7 ± 0.2%	−18.1 ± 1.9%	−18.1 ± 1.9%	−18.1 ± 1.9%	−18.1 ± 1.9%	−18.1 ± 1.9%	−18.1 ± 1.9%
1 week ($n = 1$)	120.1 ± 71.7	9.8 ± 2.1%	−10.7 ± 0.3%	2.5 ± 0.1%	−5.4 ± 0.1%	−6.8 ± 1.7%	−9.0 ± 0.2%	0.4 ± 0.1%
2 weeks ($n = 5$)	164.4 ± 78.2	20.2 ± 3.5%	47.2 ± 1.0%	19.1 ± 0.3%	7.4 ± 0.2%	6.1 ± 0.1%	16.9 ± 0.4%	28.9 ± 0.8%
4 weeks ($n = 1$)	167.3 ± 78.3	12.6 ± 5.4	40.0 ± 1.1%	18.5 ± 0.6%	−1.8 ± 0.1%	−1.7 ± 0.1%	16.6 ± 0.6%	20.9 ± 0.8%

Average grayscale value (GV) of the entire μCT image slice for each preparation regime is listed in first data column. CNS, central nervous system; M, myelinated; nM, non-myelinated; PNS, peripheral nervous system.

alligator reported on by Tsai and Holliday (2011) and George and Holliday (2013), from which these authors were able to successfully reconstruct the jaw adductor musculature, the associated cartilago transiliens, and portions of the trigeminal nerve. After 2 weeks of staining, we found that both superficial and deep soft tissues of the head could be visualized clearly. The μCT scans of our 2-week preparations (Fig. 1C) thus reveal a far greater range of soft-tissue structures than has been reported previously using i-e μCT to image post-embryonic vertebrates (Figs. 2A, 3, and 4A,B). At 4 weeks, our specimens seemed to have become oversaturated with iodine (Fig. 1D), which resulted in markedly reduced contrast in μCT images. Although soft-tissue anatomy could still be readily appreciated after 4 weeks of staining, we found the levels of contrast to be visually inferior compared to those in 2-week specimens. For our larger emu heads, however, we found 4 weeks in Lugol's iodine solution to be optimal (Figs. 2B and 4C,D), resulting in contrast levels and tissue differentiation comparable to those seen in our 2-week stained alligator specimens (Figs. 2A and 4A,B).

We confirmed these qualitative interpretations empirically by testing for differences in contrast in the i-e μCT images for homologous structures across our four preparation regimes (see Table 2). For our 2-week stained specimens, we found that fat and skeletal muscle had the highest mean contrast levels at 47.2 ± 1.0% and 28.9 ± 0.8%, respectively (i.e., approximately 47% and 29% brighter than the average brightness of the entire μCT TIFF slice). Glandular and myelinated peripheral nervous system tissues showed intermediate values of 19.1 ± 0.3% and 16.9 ± 0.4%, respectively. Non-myelinated tissues of both the central and peripheral nervous systems had the lowest contrast values at 7.4 ± 0.2% and 6.1 ± 0.1%, respectively.

A particularly surprising finding was the differential staining that we observed within certain skeletal muscles, namely those of the alligator jaw adductor system, a phenomenon that has not been reported in previous i-e μCT studies as far as we are aware. Our data clearly show bilaterally symmetrical regions of relative brightness and darkness within certain jaw adductor muscles, as seen in our frontal μCT slices (see Figs. 2A, right and 3B). We suggest that these variations correspond to differences in muscle physiology, specifically reflecting the carbohydrate load of white (glycolytic) versus red (oxidative) musculature (i.e., those muscle fibers that are brighter versus darker in i-e μCT images, respectively). For example it is known that the *M. adductor mandibulae externus superficialis* (mames) of the American alligator is fairly white (Gignac, 2010), containing ~48.9% glycolytic fibers (a higher proportion than any other fiber type; Sato et al., '92), whereas the deep portion of the *M. pterygoideus dorsalis* (mptd) is largely red (Gignac, 2010), containing ~65.5% oxidative fibers (as compared to just ~9.0% glycolytic fibers; Sato et al., '92). Corresponding to these patterns, the mames imaged nearly white in our i-e μCT scans, whereas the mptd was much darker, indicating that the former bound substantially more iodine

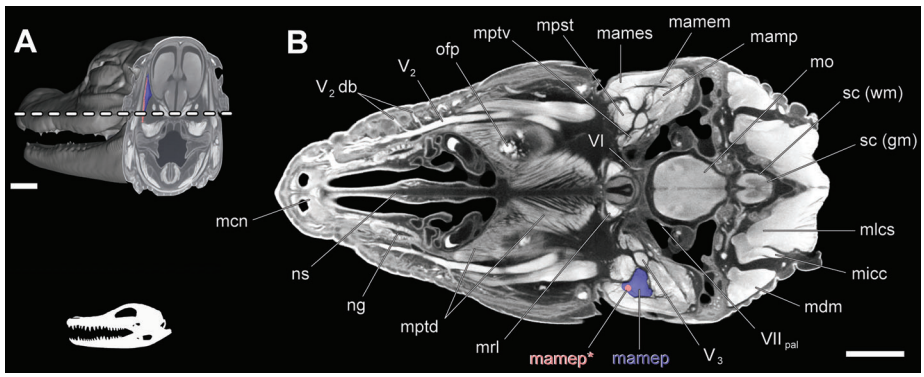

Figure 3. X-ray μCT slices through the head of a post-hatchling American alligator (*Alligator mississippiensis*) (21.5 mm head width) stained in an 11.25% Lugol's iodine (I_2KI) solution for 2 weeks. The volume rendering in (**A**) is sliced posteriorly in a transverse plane through the jaw adductor chamber. On the right is a frontal slice (**B**), taken at the level indicated by the dashed line in (A), illustrating a subset of the diversity of soft tissues that can be readily differentiated via iodine-enhanced μCT imaging. In both (A) and (B), a single fascicle (pink) has been segmented out of one of the jaw adductor muscles (mamep; purple) to illustrate how certain aspects of muscle morphology (e.g., fascicle length, fiber angle) can be visualized for quantification using this technique. (Note also the [unsegmented] individual fascicles clearly visible within mptd near the midline.) Scale bars = 0.5 cm. mamem, *M. adductor mandibulae externus medialis*; mamep, *M. adductor mandibulae externus profundus*; mamep*, individual segmented fascicle of *M. adductor mandibulae externus profundus*; mames, *M. adductor mandibulae externus superficialis*; mamp, *M. adductor mandibulae posterior*; mcn, *M. constrictor naris*; mdm, *M. depressor mandibulae*; micc, *M. iliocostalis capitis*; mlcs, *M. longissimus capitis superficialis*; mo, medulla oblongata; mpst, *M. pseudotemporalis*; mptd, *M. pterygoideus dorsalis*; mptv, *M. pterygoideus ventralis*; mrl, *M. rectus lateralis*; ofp, orbital fat pad; ng, nasal gland; ns, nasal septum; sc (gm), spinal cord gray matter; sc (wm), spinal cord white matter; V_2, maxillary division of trigeminal nerve; V_2 db, dental branches of maxillary division of trigeminal nerve; V_3, mandibular division of trigeminal nerve; VI, abducens nerve; VII_{pal}, palatine ramus of facial nerve.

than the latter (Fig. 3). This pattern is consistent with the known higher carbohydrate content of white skeletal muscle tissue such as the alligator mames (Sato et al., '92). Thus, i-e μCT may provide a rapid means of identifying regional patterns of variation in muscle physiology, while simultaneously facilitating the visualization of gross myological features.

DISCUSSION

Methodological Differences From Previous Studies

To improve soft-tissue visualization in post-embryonic vertebrate specimens, we opted to increase both the concentration of the contrast agent used for staining and the peak accelerating voltage of the X-ray tube used during μCT scanning. We used an 11.25% solution of Lugol's iodine. The staining protocols used in prior studies have been reported in several different ways, with stain concentrations characterized by some workers as percentages of I_2KI (i.e., total solute weight per volume [w/v]; Cox and Jeffery, 2011; Jeffery et al., 2011), by others as percentages of I_2 alone (w/v; Metscher, 2009a,b), and in some cases, not at all (e.g., Herdina et al., 2010; Tsai and Holliday, 2011; George and Holliday, 2013). Nonetheless, the reported concentrations used in previous studies have typically been 1.5–37.5 times lower than those used in this study (for exceptions, see Jeffery et al. (2011) and Cox and Jeffery (2011)). In addition, many of the specimens examined in previous studies were stained on the order of hours (Metscher, 2009a,b) or days (Tobita et al., 2010; Jeffery et al., 2011; Tsai and Holliday, 2011) instead of weeks, as done here (and for specimens imaged by Jeffery et al. (2011) and Cox and Jeffery (2011)). Thus, the sample organisms prepared and imaged for this study were imbued with substantially more iodine than has been typical in most previous studies. Given the greater amount of contrast agent, we also sought to scan our specimens with a more powerful μCT imaging system. All specimens in this study were scanned at peak voltages of 130–200 kV, which are 1.6–9.1 times higher than the 22–80 kV typically employed to examine contrast-enhanced invertebrates (Metscher, 2009a), vertebrate embryos (Metscher, 2009a,b), and intact heads of post-embryonic vertebrates (Metscher, 2009a,b; Jeffery et al., 2011; Tsai and Holliday, 2011). The one exception, however, is a relatively large squirrel head scanned at 195 kV after 7 weeks of immersion in 25% I_2KI (i.e., 8.33% w/v of I_2) (Jeffery et al., 2011). In addition, Cox and Jeffery (2011) reported using a μCT system with a maximum tube voltage of 320 kV to generate impressive i-e μCT images of additional rodent specimens. Taken together, it appears that the outstanding soft-tissue images that we report on here, as well as those demonstrated by Cox and Jeffery (2011) and Jeffery et al. (2011), are directly attributable to the combination of increased

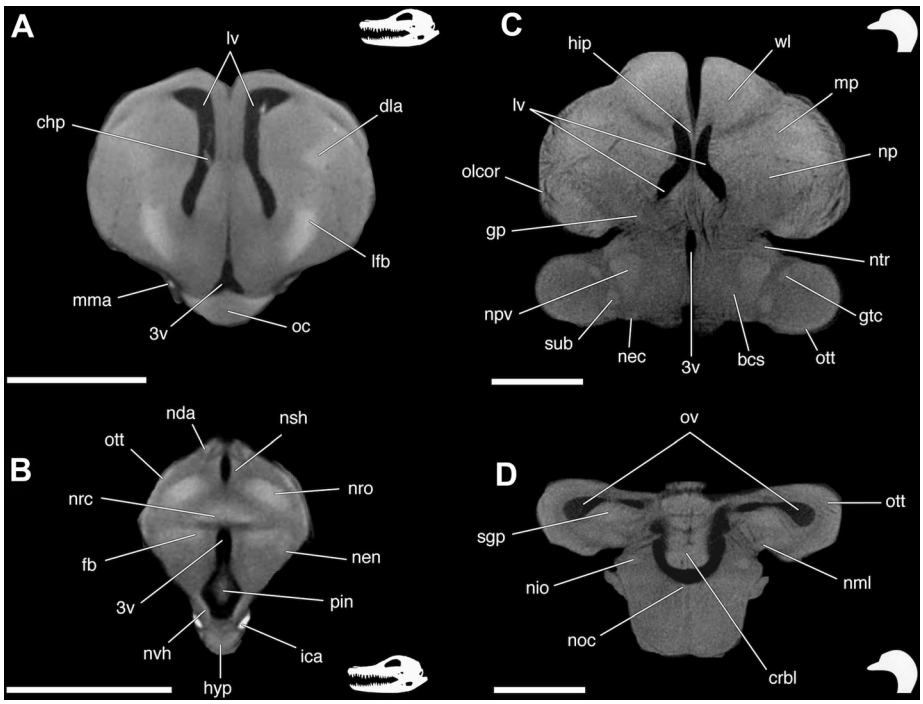

Figure 4. Transverse X-ray μCT slices through the brains of a post-hatchling American alligator (*Alligator mississippiensis*; **A** and **B**) and post-hatchling emu (*Dromaius novaehollandiae*; **C** and **D**), illustrating the effects of Lugol's iodine (I_2KI) staining on the imaging and differentiation of neuroanatomical structures within the telencephalon (A,C), mesencephalon (B,C,D), and rhombencephalon (D). Scale bars = 0.5 cm. 3v, third ventricle; bcs, brachium colliculi superioris; chp, choroid plexus; crbl, cerebellum; dla, dorso-lateral area; fb, forebrain bundle; gp, globus pallidum; gtc, griseum tectale; hip, hippocampus; hyp, hypophysis; ica, internal carotid artery; lfb, lateral forebrain bundle; lv, lateral ventricles; mma, middle meningeal artery; mp, mesopallium; nda, nucleus dorsomedialis anterior; nec, nucleus ectomammalliaris; nen, nucleus entopeduncularis; nio, nucleus isthmo-opticus; nml, nucleus mesencephalicus lateralis (pars dorsalis); noc, nucleus oculomotoris; np, nidopallium; npv, nucleus posteroventralis; nrc, nucleus reuniens pars centralis; nro, nucleus rotundus; nsh, nucleus subhabenularis; ntr, nucleus triangularis; nvh, nucleus ventralis hypothalami; oc, optic chiasm; olcor, olfactory cortex; ott, optic tectum; ov, optic ventricles; pin, pineal gland; sgp, stratum griseum periventricularis; sub, subpraetectalis; wl, wulst (hyperpallium).

levels of iodine in soft tissues (due to stronger concentrations and longer staining periods) and substantially higher X-ray-tube accelerating voltages used for μCT scanning. Thus, future studies should target this combination to visualize more fully the soft-tissue anatomy of post-embryonic vertebrates.

It bears noting that our recommendations may appear to contradict those of Vickerton et al. (2013), who clearly documented tissue shrinkage at relatively high concentrations of Lugol's iodine solution for small samples of isolated soft tissues. However, we believe that our results add an additional dimension to their findings. Vickerton et al. (2013) conclude—and we broadly agree—that well-imaged specimens are those which maximize staining concentration while minimizing shrinkage artifacts. Our results indicate that larger, more voluminous specimens require longer incubation periods in Lugol's iodine solution for complete tissue staining but generally do exhibit significant shrinkage. We suspect that the surface areas over which osmosis occurs may be a limiting factor when specimen volume is relatively high, as is often the case with post-embryonic specimens. In such cases, greater exposure to Lugol's iodine solution seems to be required to achieve sufficient uptake necessary for well-contrasted CT images. Our well-contrasted specimens, however, do not show the extremes of soft-tissue shrinkage (up to 60% by volume) demonstrated in the Vickerton et al. (2013) study (as illustrated in Fig. 2). Thus, we recommend that the concentration of Lugol's iodine used for specimen preparation should be scaled with consideration to specimen volume.

Effects of Varying Staining Durations

Among our sample of post-hatchling alligator heads, the highest levels of soft-tissue contrast were recorded in the 2-week stained specimens (see Table 2). Not surprisingly, these also showed the greatest degree of visual clarity among our staining preparations (see Fig. 1). Similar tissue types within these specimens, such as

non-myelinated nervous tissues, located both internal and external to the braincase (a potential physical barrier to iodine penetration), showed similar values of average contrast after 2 weeks of staining (Table 2). This indicates that after 2 weeks in I_2KI, iodine absorption generally occurred evenly throughout the heads of our specimens.

μCT scans of the emu head stained in Lugol's solution for 4 weeks revealed levels of tissue differentiation comparable to those observed in our alligator heads stained for 2 weeks (Figs. 2 and 4). The emu heads were larger, and presumably more time was necessary for complete iodine penetration. Nonetheless, muscles, exocrine glands, myelinated and non-myelinated nervous tissues, fat deposits, and epithelial structures, as well as keratinized tissues such as the beak and feathers, were all readily distinguishable. The similar quality of these images thus indicates the potential feasibility of direct comparisons of cephalic soft-tissue anatomy between morphologically disparate taxa via i-e μCT imaging.

The Utility of i-e μCT

The primary utility of i-e μCT lies in facilitating rapid and detailed imaging of complex, three-dimensional soft-tissue anatomy. Examples of all major tissue types of the head were clearly visualized in our exemplar specimens of both alligators and emus (see Figs. 2–4). Remarkably, because i-e μCT permits the differentiation of myelinated and non-myelinated nervous tissues, it even makes possible the visualization of nuclei, striata, and tracts within the brain (Fig. 4). In addition, such imaging can be achieved without encephalectomy, allowing for the interrelationships between central and peripheral components of the nervous system of the head to be preserved (Fig. 2). These kinds of data thus have the potential to open up new avenues of study using 3D rendering software to quantify and compare neuroanatomical structures among different body regions and species.

In addition to neuroanatomy, detailed 3D reconstructions of skeletal muscles make accessible important details of functional morphology, such as whole-muscle volumes, fiber orientations, fascicle lengths, pennation angles, and attachment sites—in even the smallest of specimens. These data can facilitate the reconstruction of biomechanically relevant musculoskeletal parameters such as physiological cross-sectional area and lever-arm lengths. For example, Jeffery et al. (2011) used an i-e μCT-based rodent masseter model to demonstrate that individual muscle fascicles can be readily isolated using this technique, and we also find this to be the case in our archosaur data set (Fig. 3). Furthermore, i-e μCT is amenable to reconstructing the interrelationships of multiple, complex soft-tissue systems in 3D to understand better how these systems relate to one another anatomically. To demonstrate this, we reconstructed the brain, a sample of six extrinsic ocular muscles, the olfactory tracts and bulbs, and the five cranial nerves that pass through the orbit for one of our 2-week stained alligator specimens (Fig. 5). A primary advantage of such reconstructions is in the retention of anatomical fidelity for complexly organized, delicate structures such as thin, overlapping muscles and nerve branches, whose relationships can often be disturbed, obscured, or destroyed during gross dissection.

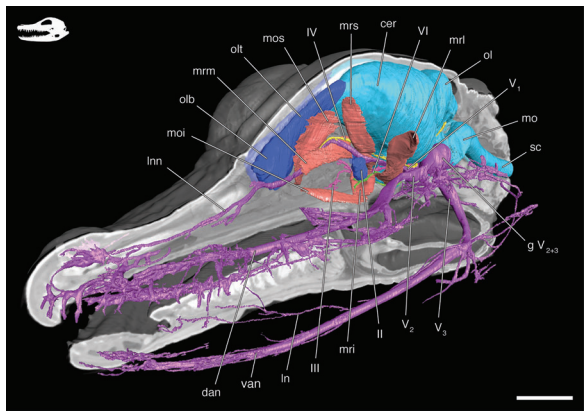

Figure 5. Anterolateral view of a three-dimensional reconstruction of the brain and selected cranial nerves and extrinsic ocular muscles, based on digital segmentation of these structures in an iodine-enhanced μCT scan of a post-hatchling American alligator (*Alligator mississippiensis*). The left half of the skull has been removed digitally from this rendering to facilitate visualization of the reconstructed soft-tissue structures; however, the right half of the skull has been left in place as an anatomical frame of reference. Color key: brain, turquoise; olfactory tract and bulb and optic nerve, blue; oculomotor nerve, pink; trochlear nerve, yellow; trigeminal nerve and associated ganglia and branches, purple; abducens nerve, green; extrinsic ocular muscles, salmon. Scale bar = 0.5 cm. cer, cerebrum; dan, dorsal alveolar nerve; g V_{2+3}, maxillomandibular ganglion; ln, lingual nerve; lnn, lateral nasal nerve; mo, medulla oblongata; moi, *M. obliquus inferior*; mos, *M. obliquus superior*; mri, *M. rectus inferior*; mrl, *M. rectus lateralis*; mrm, *M. rectus medialis*; mrs, *M. rectus superior*; olb, olfactory bulb; olt, olfactory tract; ol, optic lobe; sc, spinal cord; van, ventral alveolar nerve; II, optic nerve; III, oculomotor nerve; IV, trochlear nerve; V_1, ophthalmic division of trigeminal nerve; V_2, maxillary division of trigeminal nerve; V_3, mandibular division of trigeminal nerve; VI, abducens nerve.

The Future of i-e μCT

The process of preparing specimens for i-e μCT imaging is extremely straightforward, simply involving immersion in Lugol's iodine solution following fixation. The results, however, are quite extraordinary. The results presented here, as well as those recently published by other authors (e.g., Metscher, 2009a,b; Cox and Jeffery, 2011; Jeffery et al., 2011), demonstrate that i-e μCT

represents a major methodological advance in the field of vertebrate morphology, the potential of which has only begun to be explored. Subsequent steps to further refine this tool will involve increasing taxonomic sampling, determining how to fully stain progressively larger specimens, calibrating staining and scanning parameters to optimally target specific tissue types, and resolving the potential physiological signal associated with the differential staining of fast- versus slow-twitch muscle fibers. We anticipate that i-e μCT will generate new, substantial, high-quality data for functional morphologists (e.g., length, area, volume, and mass parameters for biomechanical analyses; Tsai and Holliday, 2011), descriptive anatomists (e.g., appreciation of spatial relationships and integration of disparate anatomical systems; Jeffery et al., 2011), and systematists (e.g., identification of phylogenetically informative soft-tissue anatomical characters deep within the body), among others. Collectively, the exploration of this technique so far represents just a fraction of the possibilities that it offers. Iodine-enhanced μCT holds the potential to become an extraordinarily valuable research platform that will likely facilitate remarkable new discoveries as it is adopted by a wider range of evolutionary morphologists.

ACKNOWLEDGMENTS

We thank N. S. Jeffery (University of Liverpool), B. D. Metscher (University of Vienna), G. R. Gindi (Stony Brook University [SBU]), and F. A. Dilmanian (Brookhaven National Laboratory) for feedback on staining and μCT imaging protocols; M. A. Norell (American Museum of Natural History [AMNH]), A. H. Turner (SBU), J. Thostenson (AMNH), M. Hill (AMNH), M. E. Gold (AMNH), and A. Watanabe (AMNH) for access to and use of the Microscopy and Imaging facility at the AMNH and use of computer workstations; R. M. Elsey (Louisiana Department of Fisheries and Wildlife) and A. M. Richmond (University of Massachusetts) for assistance in procuring specimens; B. A. Patel (University of Southern California) for technical assistance with Avizo; and G. M. Erickson (Florida State University), A. H. Turner (SBU), A. Balanoff (SBU), D. W. Krause (SBU), H. D. O'Brien (Ohio University [OU]), S. H. Burch (OU), and two anonymous reviewers for thoughtful feedback during the preparation of this manuscript. This work was supported financially by the National Science Foundation (NSF IOS-0749750; N.J.K.) and the Stony Brook University Department of Anatomical Sciences (P.M.G. and N.J.K.).

LITERATURE CITED

Bloch JI, Silcox MT. 2006. Cranial anatomy of the Paleocene plesiadapiform *Carpolestes simpsoni* (Mammalia, Primates) using ultra high-resolution X-ray computed tomography, and the relationships of plesiadapiforms to euprimates. J Hum Evol 50:1–35.

Bock WJ, Shear CR. 1972. A staining method for gross dissection of vertebrate muscles. Anat Anz 30:222–227.

Brainerd EL, Baier DB, Gatesy SM, et al. 2010. X-ray reconstruction of moving morphology (XROMM): precision, accuracy and applications in comparative biomechanics research. J Exp Zool 313A:262–279.

Cox PG, Jeffery N. 2011. Reviewing the morphology of the jaw-closing musculature in squirrels, rats, and guinea pigs with contrast-enhanced micro-CT. Anat Rec 294:915–928.

Cox PG, Fagan MJ, Rayfield EJ, Jeffery N. 2011. Finite element modeling of squirrel, guinea pig and rat skulls: using geometric morphometrics to assess sensitivity. J Anat 219:696–709.

Degenhardt K, Wright AC, Horng D, Padmanabhan A, Epstein JA. 2010. Rapid 3-D phenotyping of cardiovascular development in mouse embryos by micro-CT with iodine staining. Circ Cardio Imaging 3:314–322.

Düring DN, Ziegler A, Thompson CK, et al. 2013. The songbird syrinx morphome: a three-dimensional, high-resolution, interactive morphological map of the zebra finch vocal organ. BMC Biol 11:1.

Faulwetter S, Vasileiadou A, Kouratoras M, Dailianis T, Arvanitidis C. 2013. Micro-computed tomography: Introducing new dimensions to taxonomy. ZooKeys 263:1–45.

Gauthier JA, Kearney M, Maisano JA, Rieppel O, Behlke ADB. 2012. Assembling the squamate tree of life: perspectives from the phenotype and the fossil record. Bull Peabody Mus Nat Hist 53:3–308.

George ID, Holliday CM. 2013. Trigeminal nerve morphology in *Alligator mississippiensis* and its significance for crocodyliform facial sensation and evolution. Anat Rec 296:670–680.

Gignac PM. 2010. Biomechanics and the ontogeny of feeding in the American alligator (*Alligator mississippiensis*): reconciling factors contributing to intraspecific niche differentiation in a large-bodied vertebrate [Ph.D. dissertation]. Florida State University, Tallahassee, FL, USA, p 184.

Headrick TC. 2010. Statistical simulation: power method polynomials and other transformations. Boca Raton, FL: Chapman and Hall.

Herdina AN, Herzig-Straschil B, Hilgers H, Metscher BD, Plenk H Jr. 2010. Histomorphology of the penis bone (baculum) in the gray long-eared bat *Pleocotus austriacus* (Chiroptera, Vespertilionidae). Anat Rec 293:1248–1258.

Jeffery N, Stephenson RS, Gallagher JA, Jarvis JC, Cox PG. 2011. Micro-computed tomography with iodine staining resolves the arrangement of muscle fibres. J Biomech 44:189–192.

Metscher BD. 2009a. Micro-CT for comparative morphology: simple staining methods allow high-contrast 3-D imaging of diverse non-mineralized animal tissues. BMC Physiol 9:11.

Metscher BD. 2009b. Micro-CT for developmental biology: a versatile tool for high-contrast 3-D imaging at histological resolutions. Dev Dynam 238:632–640.

Moazen M, Curtis N, O'Higgins P, et al. 2008. Assessment of the role of sutures in a lizard skull: a computer modeling study. Proc Roy Soc B 276:39–46.

Pauwels E, Van Loo D, Cornillie P, Brabant L, Van Hoorebeke L. 2013. An exploratory study of contrast agents for soft tissue visualization by

means of high resolution X-ray computed tomography imaging. J Microsc 250:21–31.

Rae TC, Koppe T, Spoor F, Benefit B, McCrossin M. 2002. Ancestral loss of the maxillary sinus in Old World monkeys and independent acquisition in *Macaca*. Am J Phys Anth 117:293–296.

Rayfield EJ, Norman DB, Horner CC, et al. 2001. Cranial design and function in a large theropod dinosaur. Nature 409:1033–1037.

Rhodes JS, Ford TR, Lynch JA, Liepins PJ, Curtis RV. 1999. Micro-computed tomography: a new tool for experimental endodontology. Intl Endo J 32:165–170.

Ross CF. 2005. Finite element analysis in vertebrate biomechanics. Anat Rec 283A:253–258.

Sato I, Shimada K, Sato T, Kitigawa T. 1992. Histochemical study of jaw muscle fibers in the American alligator (*Alligator mississippiensis*). J Morph 211:187–199.

Stephenson RS, Boyett MR, Hart G, et al. 2012. Contrast enhanced micro-computed tomography resolves the 3-dimensional morphology of the cardiac conduction system in mammalian hearts. PLoS ONE 7:e35299.

Tobita K, Liu X, Lo CW. 2010. Imaging modalities to assess structural birth defects in mutant mouse models. Birth Defects Res C 90:176–184.

Tsai HP, Holliday CM. 2011. Ontogeny of the *Alligator* cartilago transiliens and its significance for sauropsid jaw muscle evolution. PLoS ONE 6:e24935.

van Rietbergen B, Weinans H, Huiskes R, Odgaard A. 1995. A new method to determine trabecular bone elastic properties and loading using micromechanical finite element models. J Biomech 28:69–81.

Vickerton P, Jarvis J, Jeffery N. 2013. Concentration-dependent specimen shrinkage in iodine-enhanced microCT. J Anat 223:185–193.

Witmer LM. 2004. Palaeontology: inside the oldest bird brain. Nature 430:619–620.

Witmer LM, Ridgely RC, Dufeau DL, Semones MC. 2008. Using CT to peer into the past. In: Endo H, Frey R, editors. 3-D visualization of the brain and ear regions of birds, crocodiles, and nonavian dinosaurs. New York, NY: Springer. p 1–33.